Supporting Information for "Automated Detection of Short-term Slow Slip Events in Southwest Japan"

Yiming Ma[1] *, Fabien Montiel[1]

[1]Department of Mathematics and Statistics, University of Otago, Dunedin, New Zealand

Contents of this file

Texts S1, S2, S3

Figures S1, S2, S3, S4, S5, S6, S7, S8, S9, S10, S11, S12, S13, S14, S15, S16, S17

Introduction

Text S1 introduces a deterministic model to simulate SSEs.

Text S2 elaborates how to calculate $\tilde{p}_j^k$, the confidence of occurrence of SSEs.

Text S3 presents the histograms of the detected change-points for all the simulated noisy SSE data from all the different seeds and noise levels by various detection methods.

Text S4 presents the results of the other 14 identified SSEs.

Figure S1 shows the configurations of the modified model and the slip rate history.

Figure S2 shows histograms of detected change-points in all the synthetic data by SSAID and l_1 trend filtering.

*maym@maths.otago.ac.nz

Figure S3 shows histograms of detected change-points in all the synthetic data by the linear regression with ΔAIC using different thresholds.

Figure S4 shows the estimated fault model of an identified probable SSE candidate at the station 021049.

Figure S5 shows the estimated fault model of an identified probable SSE candidate at the station 950447.

Figure S6 shows the estimated fault model of an identified probable SSE candidate at the station 041133.

Figure S7 shows the estimated fault model of an identified probable SSE candidate at the station 031118.

Figure S8 shows the the estimated fault model of an identified probable SSE candidate at the station 960681.

Figure S9 shows the estimated fault model of an identified probable SSE candidate at the station 960681.

Figure S10 shows the estimated fault model of an identified probable SSE candidate at the station 021050.

Figure S11 shows the estimated fault model of an identified probable SSE candidate at the station 031124.

Figure S12 shows the estimated fault model of an identified probable SSE candidate at the station 960680.

Figure S13 shows the estimated fault model of an identified probable SSE candidate at the station 950436.

Figure S14 shows the estimated fault model of an identified probable SSE candi-

date at the station 9041134.

Figure S15 shows the estimated fault model of an identified probable SSE candidate at the station 021056.

Figure S16 shows the estimated fault model of an identified probable SSE candidate at the station 950443.

Figure S17 shows the estimated fault model of an identified probable SSE candidate at the station 021048.

Text S1. The deterministic fault model to simulate SSEs

In this section, we introduce a simplified deterministic fault model, which can spontaneously reproduce recurrent SSEs with a short duration of about a week, i.e. short-term SSEs. As shown in Fig. S1 (a), this model is composed of three sections, assuming that the velocity-weakening transition zone is embedded into two velocity-strengthening sections. The distributions of constitutive parameters (i.e. σ, D_c, a and b) in the rate- and state-dependent friction (RSF) law are shown in Fig. S1 (a) and (b). The length along the strike direction and the width along the depth direction of the model are 500 km and 80 km, respectively. The slab angle is 15°. We take $\Delta w_0 = 0.4/\sin(15^\circ)$ as its grid size and we then have $N = 200$ subfaults along the dip direction. The slip rate history of the whole new modified fault model over a period of 10 years (i.e. from the 90-th to 100-th year) is shown in Fig. S1 (c), and a one-year slip rate history of the subfault at the middle point of the VW transition is presented at Fig. S1 (d). We can see that the recurrent SSEs with short durations can spontaneously arise in the current model. All other unmentioned details about the model are the same as Ma, Anastasiou, Wang, and

Montiel (2022) (see more details therein).

Text S2. Details about hypothesis test

In this section, we elaborate more details about how to calculate $\tilde{p}_j^k$. We calculate the displacement rate at the k-th starting change-point, i.e. $\bar{v}_k^j$ in Eq. (8) of the main context, by taking the slope of the fitted linear model to the noisy data between the k-th starting and ending change-points. It takes three steps to estimate $\bar{v}_0^j$: (1) we consider the noisy SSE data as a piecewise-linear signal with $2\bar{N}_s^j$ knots; (2) we calculate the slope of each segment in the modelled piecewise-linear signal; and (3) we select the slopes which have the same sign as the secular linear process, and take their average as the estimated secular displacement rate.

It is possible that the expected B_j^k values that reject the null hypothesis depend on the sign of the secular displacement rate. If the secular displacement rate has a positive sign, at the start time of an SSE, it changes to a negative sign (see Fig. 7(a) of the main context). This indicates that negative B_j^k values are expected at the start times of SSEs. If, on the other hand, the secular displacement rate has a negative sign, positive B_j^k values are expected at the start times of SSEs. Therefore, we introduce the term of the sign function in Eq. (8) to make both cases have the same expected $\bar{B}_j^k$ values (i.e. negative). Under the null hypothesis, $\bar{B}_j^k$ follows the standard Gaussian distribution (Yano & Kano, 2022). Therefore, we estimate the probability that SSEs do not occur at the k-th starting point of the j-th station by Eq. (9) shown in the main text.

To reduce Type I errors, we combine p-values of stations neighbouring the j-th station into a new single p-value through the harmonic mean p-value method (Wilson,

2019; Yano & Kano, 2022), that is

$$\hat{p}_j^k = \frac{1}{\sum_{g=1}^{\hat{N}_a^j} (1/\mathring{p}_{j,g}^k)}, \tag{1}$$

where $\hat{N}_a^j$ is the number of stations neighbouring the j-th station, g is the neighbouring station index, and $\mathring{p}_{j,g}^k$ refers to the p-value calculated via Eq. (9) of the main text for the g-th station neighbouring the j-th station, which quantifies the probability that an SSE does not occur at the k-th starting change-point of the j-th station. Here, we refer to stations within a designated distance, denoted by D_η, from the j-th station as neighbouring stations of the j-th station. When selecting D_η, we need to guarantee that the time differences of the same detected SSE between the stations (i.e. the j-th station and its neighbouring stations) should be negligible. We have already indicated that SSAID can bear an error of at most 3 days in Section 4 of the main text, which means that the time difference should be at most 3 days. Since the average distance between stations in GEONET is about 20 km (Takagi et al., 2019) and the typical along-strike propagation velocity of ETS in our research area is $10-20$ km/day (Dragert et al., 2001; Obara, 2002, 2020), we take $D_\eta = 30$ km in our following hypothesis tests, i.e. the same as that taken by Yano and Kano (2022).

Calculating $\mathring{p}_{j,g}^k$ in Eq. (1) requires three steps: (1) we estimate the secular displacement rate $\bar{v}_0^{j,g}$ at the g-th neighbouring station of station j, by using the same approach as before; (2) we also take the slope of the fitted linear model to the noisy data at the g-th neighbouring station of the j-th station to estimate its displacement rate $\mathring{v}_k^{j,g}$ at the k-th starting change-point of the j-th station; (3) we utilize Eqs. (8) and (9) of the main text to quantify $\mathring{p}_{j,g}^k$. Note that in the second step, the period used to calculate $\mathring{v}_k^{j,g}$ is between the k-th starting and the k-th ending change-point of the j-th

station, rather than its own change-points. This is because of the assumption that an SSE should be recorded at the same time by both the j-th station and its neighbouring stations (see the explanations for choosing D_η in the last paragraph). Since the j-th station and its neighbouring stations are distributed in a nearby region, they should have similar p-values. If the k-th starting change-point at the j-th station is associated with an SSE, it is expected to have a small $\hat{p}_j^k$, so that we have high confidence to reject the null hypothesis. It is clear from Eq. (1) that $\mathring{p}_{j,g}^k$ cannot be zero. If there exists a $\mathring{p}_{j,g}^k = 0$, we manually set the associated $\hat{p}_j^k$ as 0 as we have a high probability to reject the null hypothesis.

Finally, we can obtain the confidence of the occurrence of SSEs $\tilde{p}_j^k$ via Eq. (10) in the main text.Note that when only one pair of change-points are identified (i.e. $\hat{N}_s^j = 1$), we cannot calculate $\bar{B}_j^k$ via Eq. (8) in main text and conduct the following hypothesis test instead. We assume that $\tilde{p}_j^k = 0.6$ if the sign of the displacement rate at the starting change-point is opposite to that of the secular displacement rate, otherwise $\tilde{p}_j^k = 0$. The selection of these two specific values (i.e. 0.6 and 0) is simply set for ease of discussion, based on the SSE categories defined in section 5.1.3.

Text S3. The histograms of detected change-points by different methods

In this section, we present the histograms of the detected change-points for all the simulated noisy SSE data from all the different seeds and noise levels by various detection methods (see Section 4 of the main context), including SSAID, l1 trend filtering, and the linear regression with ΔAIC, utilizing different thresholds in Figs. S2 and S3. We can see that most SSAID detections tend to converge to accurate locations with minimal errors,

demonstrating its superior detection performance. In contrast, l1 trend filtering, despite exhibiting similar behaviors, suffers from a higher number of false detections and larger errors. The results of linear regression with ΔAIC also highlight the significant influence of the chosen threshold on the detection success. When the threshold is set at a low value, the majority of detections miss the true locations, although some successful detections do occur. Conversely, raising the threshold increases the percentage of detections that correctly identify the true change-points but also introduces a higher number of false detections.

Text S4. The fault estimation results of other identified SSEs

In Section 5.2 of the main context, we indicated that 18 SSEs were identified by the fault estimation using the probable SSE candidates, while only 4 representative results were included. In this section, we present the results of the other 14 identified SSEs.

References

Dragert, H., Wang, K., & James, T. S. (2001). A silent slip event on the deeper cascadia subduction interface. *Science*, *292*(5521), 1525–1528.

Ma, Y., Anastasiou, A., Wang, T., & Montiel, F. (2022). Detecting change-points in noisy gps time series with continuous piecewise structures. *arXiv preprint arXiv:2202.12414*.

Obara, K. (2002). Nonvolcanic deep tremor associated with subduction in southwest japan. *Science*, *296*(5573), 1679–1681.

Obara, K. (2020). Characteristic activities of slow earthquakes in japan. *Proceedings of*

the Japan Academy, Series B, *96*(7), 297–315.

Okada, Y. (1985). Surface deformation due to shear and tensile faults in a half-space. *Bulletin of the Seismological Society of America*, *75*(4), 1135–1154.

Takagi, R., Uchida, N., & Obara, K. (2019). Along-strike variation and migration of long-term slow slip events in the western nankai subduction zone, japan. *Journal of Geophysical Research: Solid Earth*, *124*(4), 3853–3880.

Wilson, D. J. (2019). The harmonic mean p-value for combining dependent tests. *Proceedings of the National Academy of Sciences*, *116*(4), 1195–1200.

Yano, K., & Kano, M. (2022). l1 trend filtering-based detection of short-term slow slip events: Application to a gnss array in southwest japan. *Journal of Geophysical Research: Solid Earth*, *127*(5), e2021JB023258.

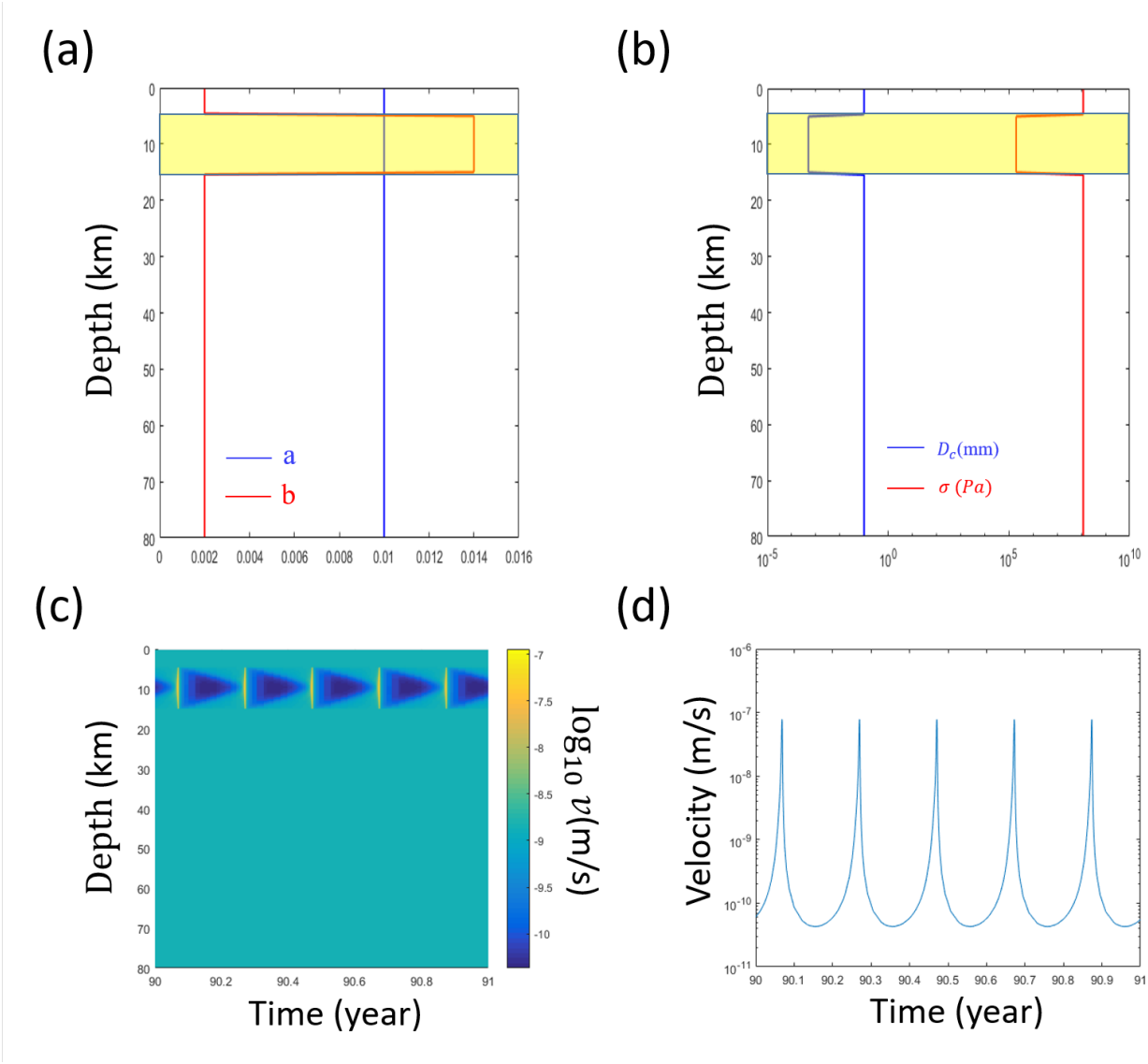

Figure S1. The spatial distribution of constitutive parameters along the depth direction in the modified reference model: (a) a and b; (b) D_c and σ. The light-yellow area refers to the VW transition zone. Slip rate history of (c) all the subfaults of the modified reference model over a 10-year period; and (d) the subfault at the middle point of the VW transition zone over a one-year period.

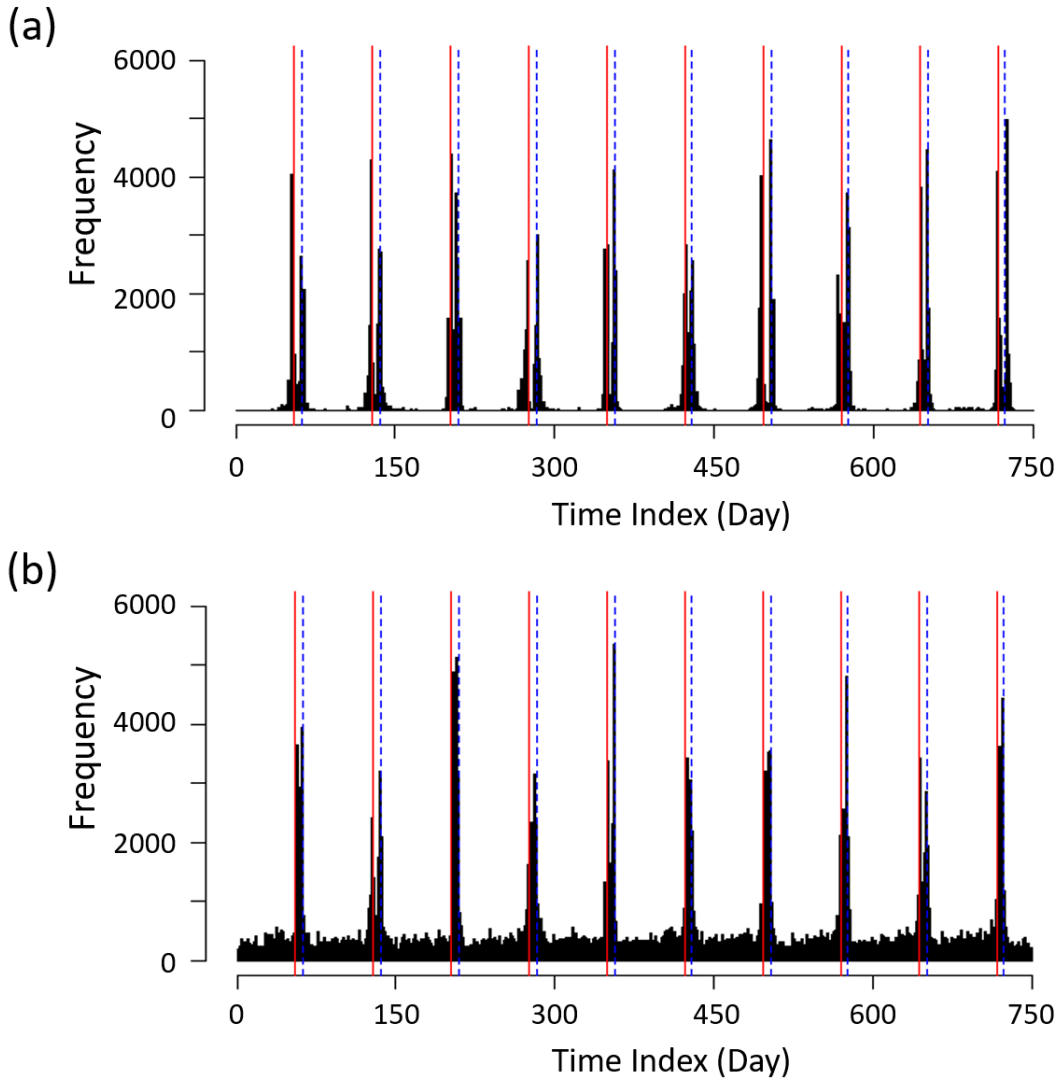

Figure S2. Histogram of detected change-points in all the synthetic data in Section 4 of the main context by different methods: (a) SSAID; (b) l_1 trend filtering. Vertical red lines: start times of simulated SSEs; vertical blue dashed lines: end times of simulated SSEs.

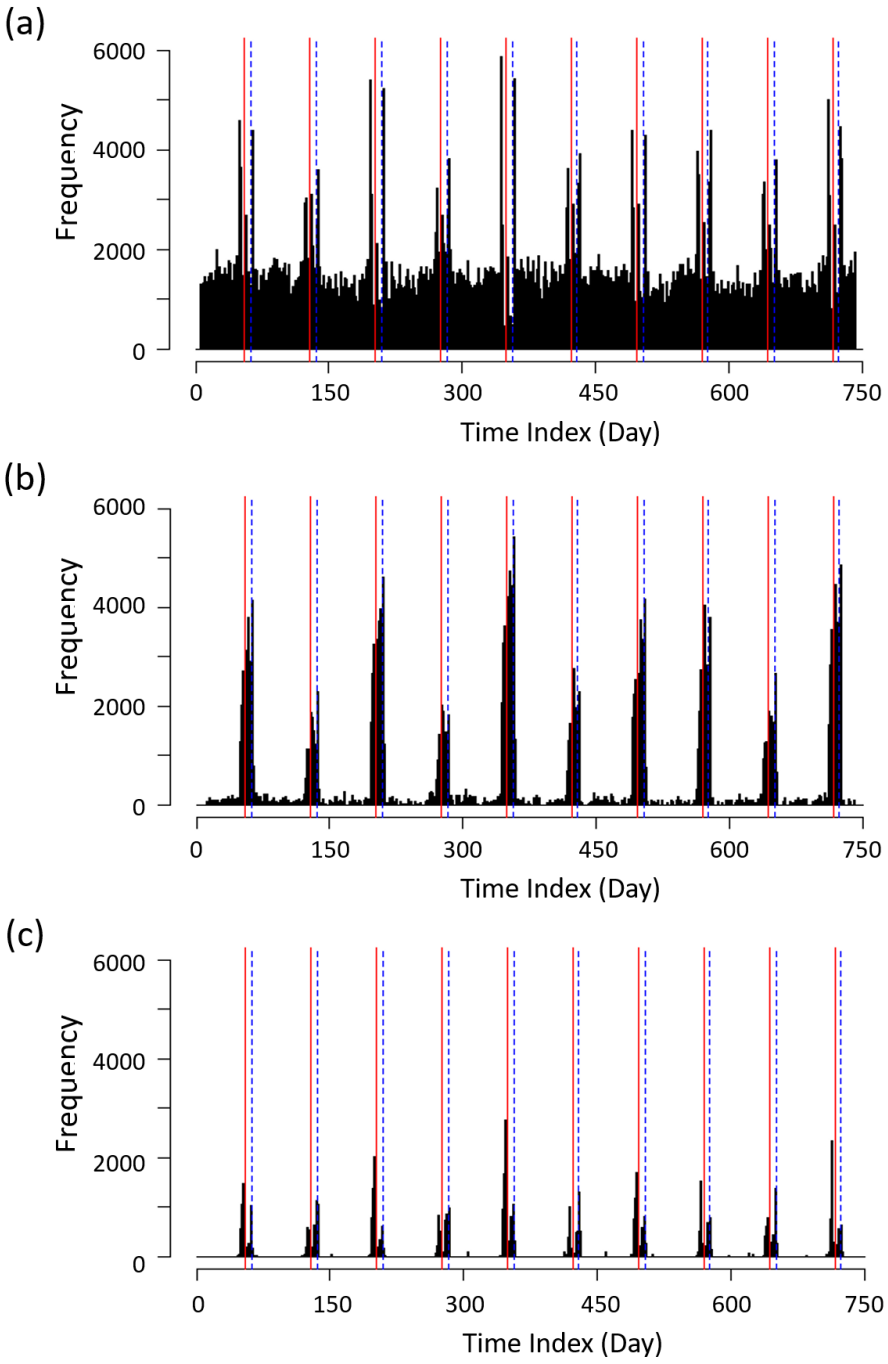

Figure S3. The same histograms as Fig. S2 but for the linear regression with ΔAIC by using different thresholds: (a) a high threshold (ζ=-10); (d) a medium threshold (ζ=-20); (e) a low threshold (ζ=-30). The sliding window is 15 days. Vertical red lines: start times of simulated SSEs; vertical blue dashed lines: end times of simulated SSEs.

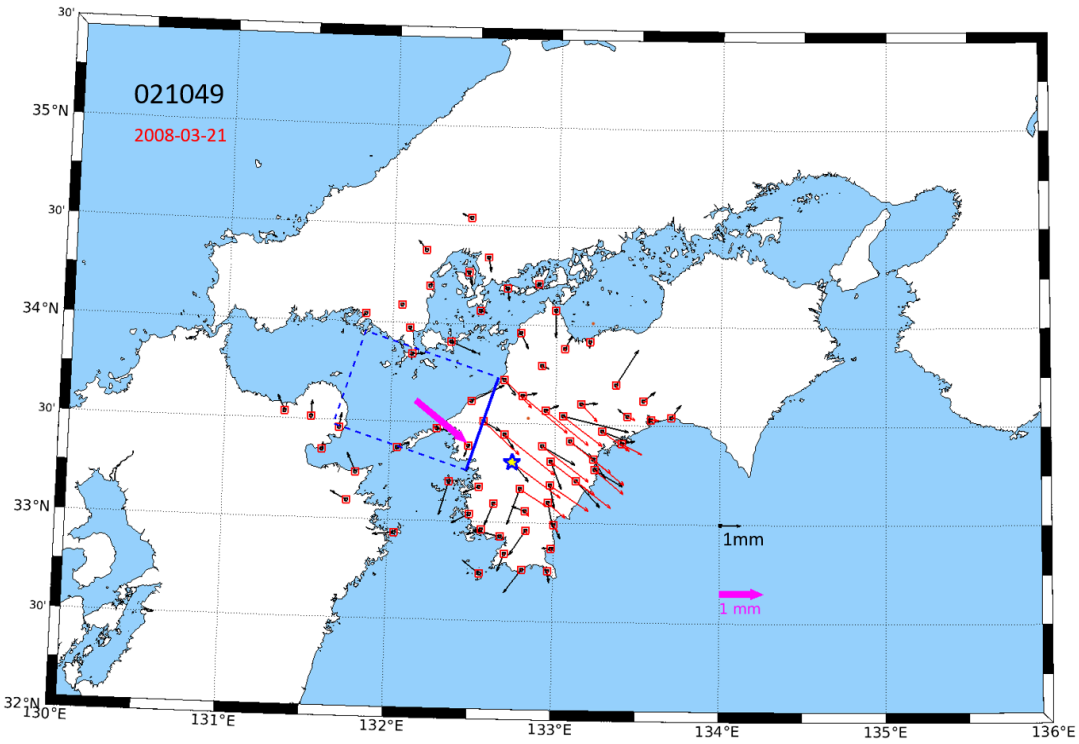

Figure S4. The estimated fault model of an identified probable SSE candidate at the station 021049. The date in red under the site name refers to the start date of this probable SSE candidate. The star in the map indicates the location of the station where this SSE candidate was identified. The black and the pink arrows in the right-bottom corner are the scale arrows for the observed displacement and the slip amount of the estimated model, respectively. The synthetic displacements by the displacement model of Okada (1985) have the same scale arrow as the observed ones. Orange dots indicate the epicentre of tremors in the episodic state 5 days before and after the date (see the date on the left-upper corner) when this candidate was found. The blue solid line of the rectangle refers to the top edge of the estimated fault model.

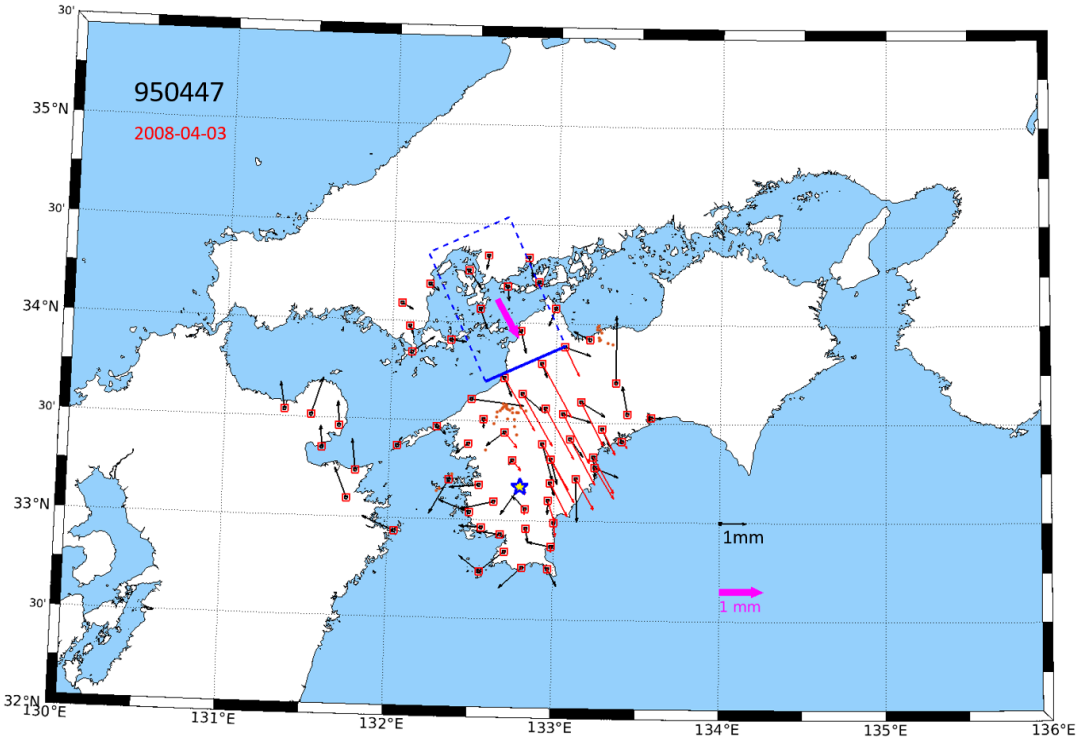

Figure S5. Same as Fig. S4 but for a probable SSE candidate at station 950447.

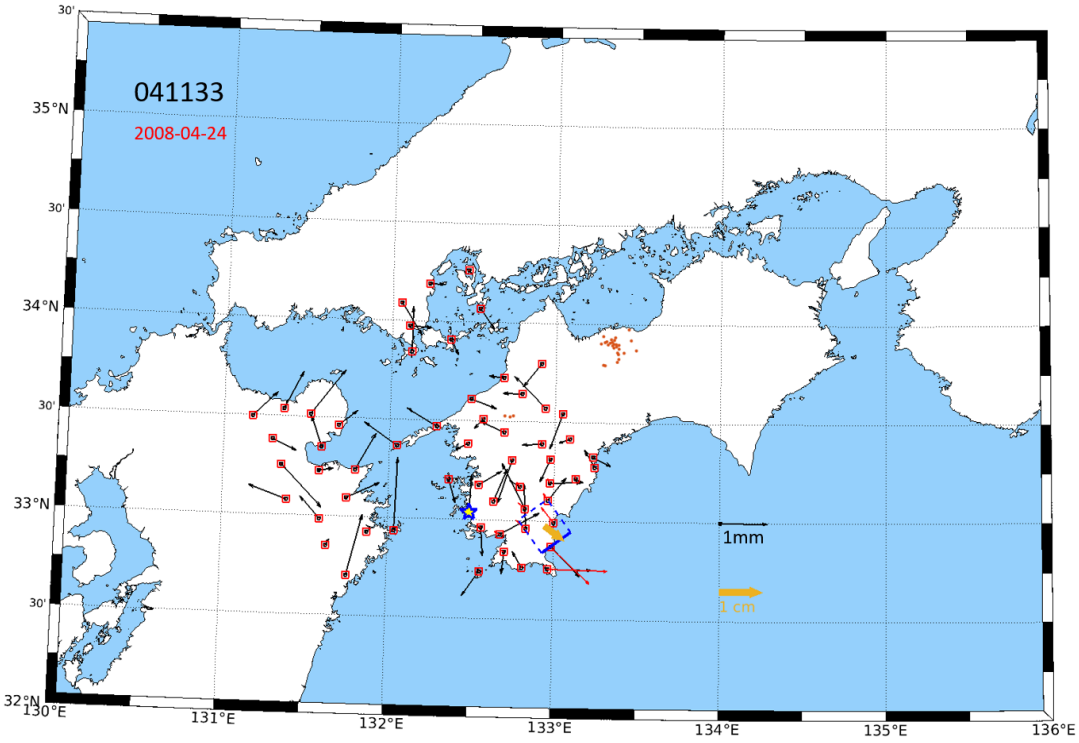

Figure S6. Same as Fig. S4 but for a probable SSE candidate at station 041133.

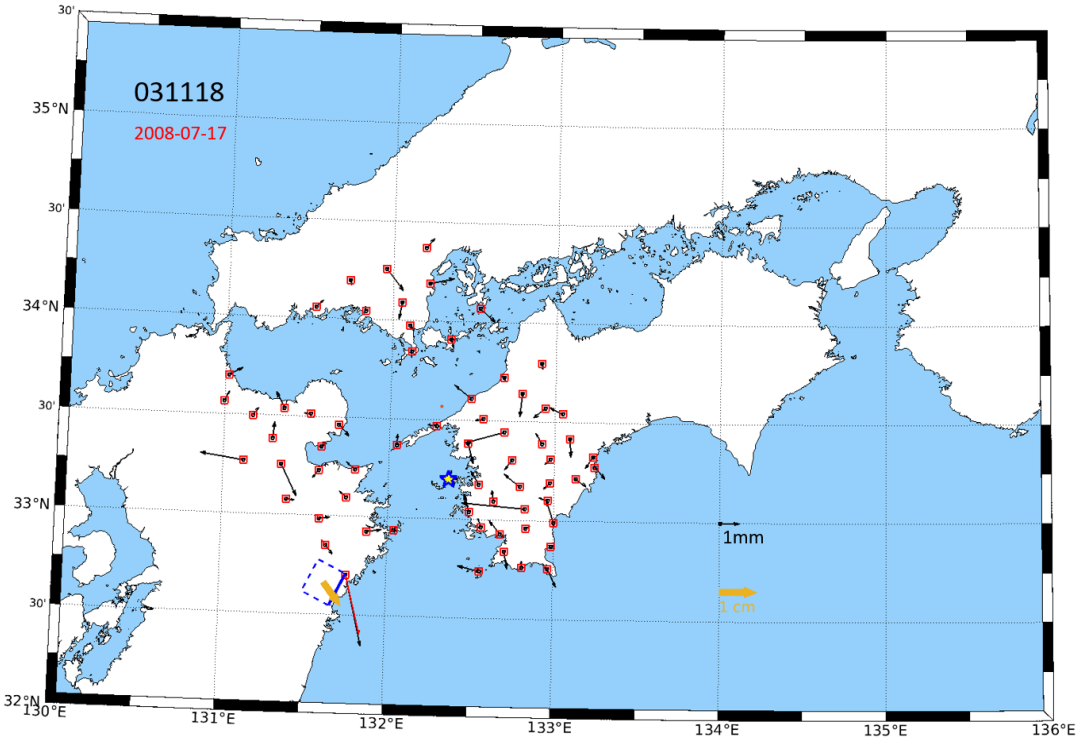

Figure S7. Same as Fig. S4 but for a probable SSE candidate at station 031118.

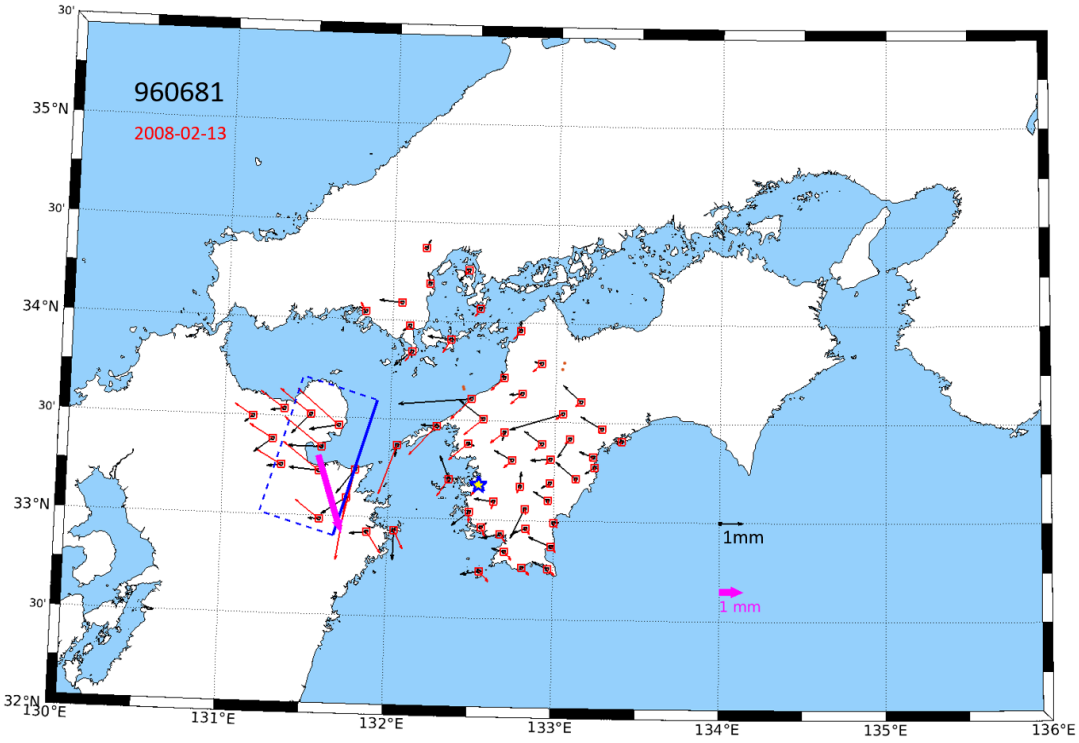

Figure S8. Same as Fig. S4 but for a probable SSE candidate at station 960681.

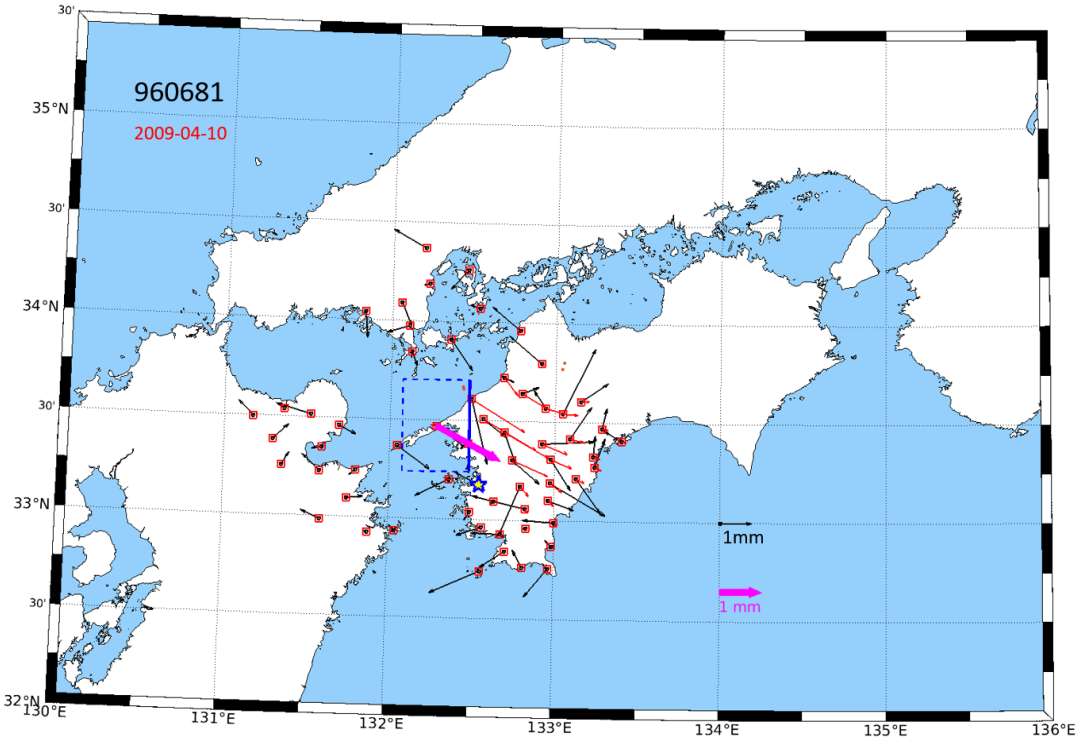

Figure S9. Same as Fig. S4 but for a probable SSE candidate at station 960681.

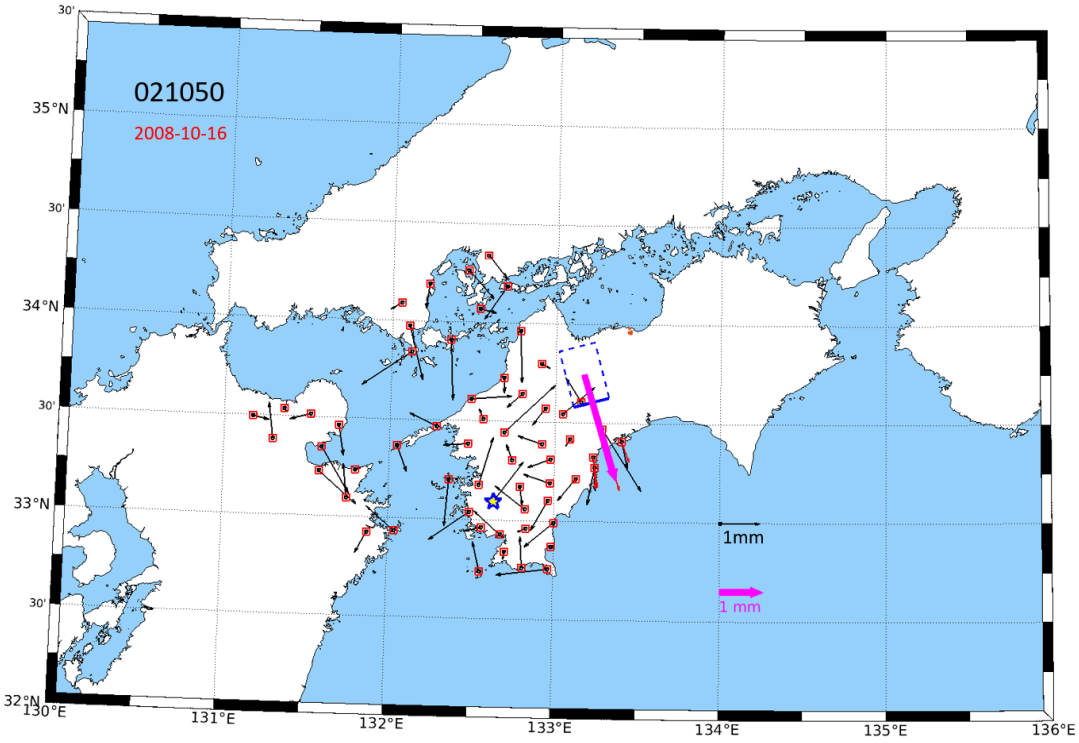

Figure S10. Same as Fig. S4 but for a probable SSE candidate at station 021050.

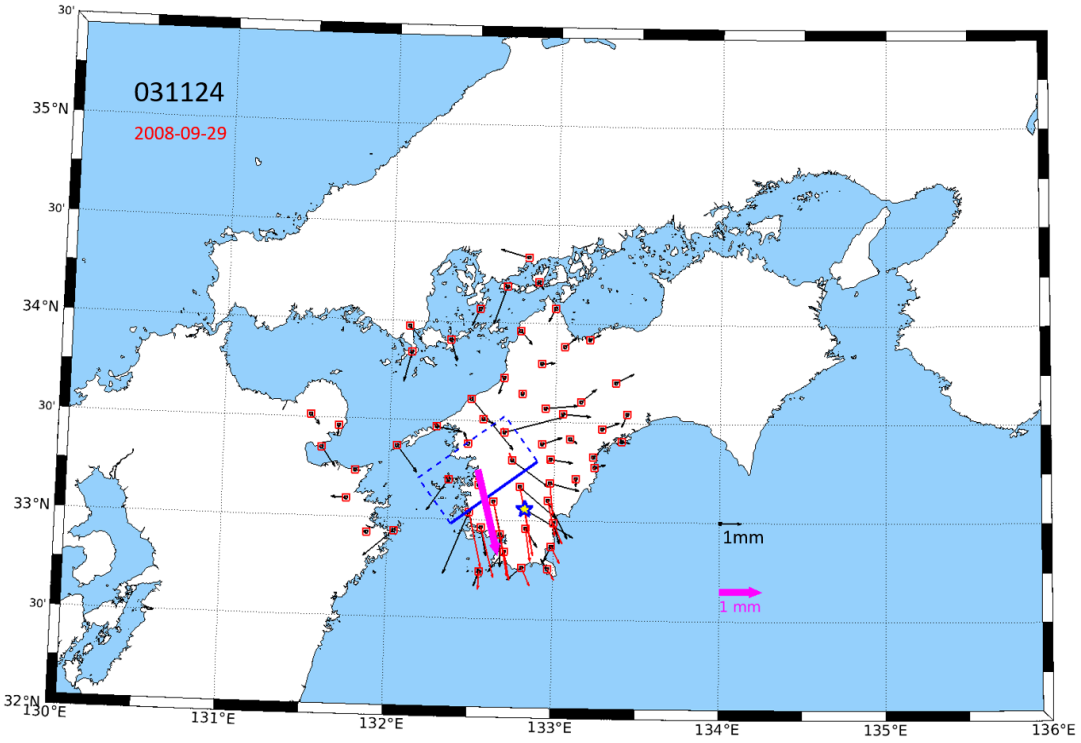

Figure S11. Same as Fig. S4 but for a probable SSE candidate at station 031124.

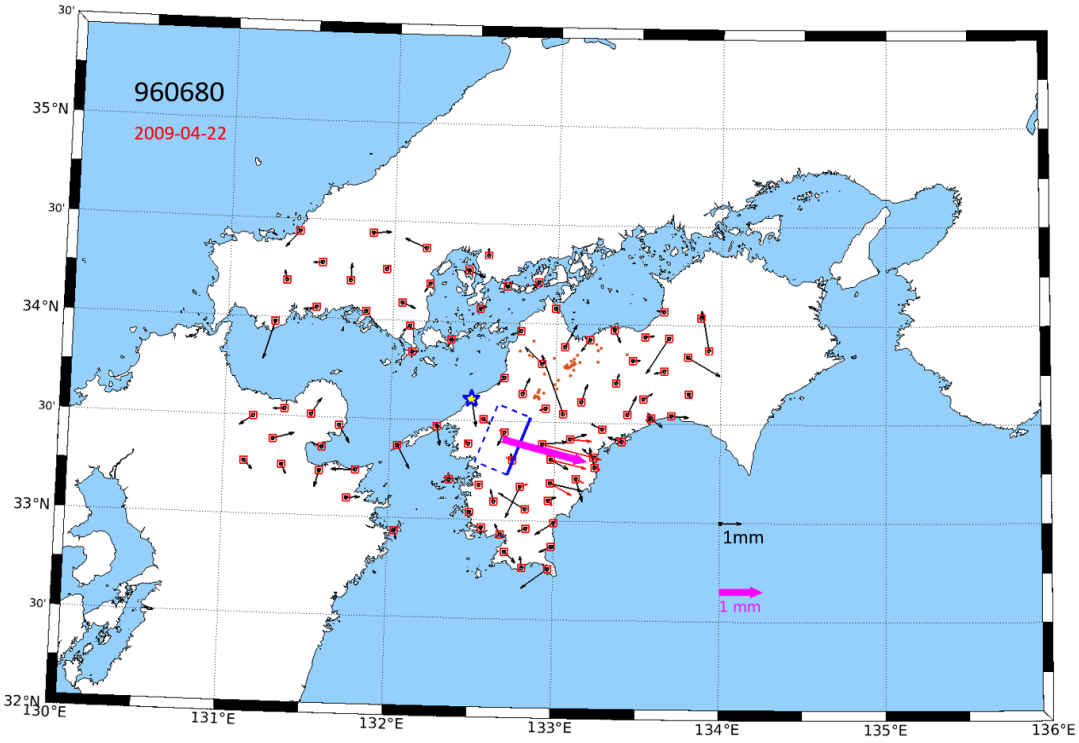

Figure S12. Same as Fig. S4 but for a probable SSE candidate at station 960680.

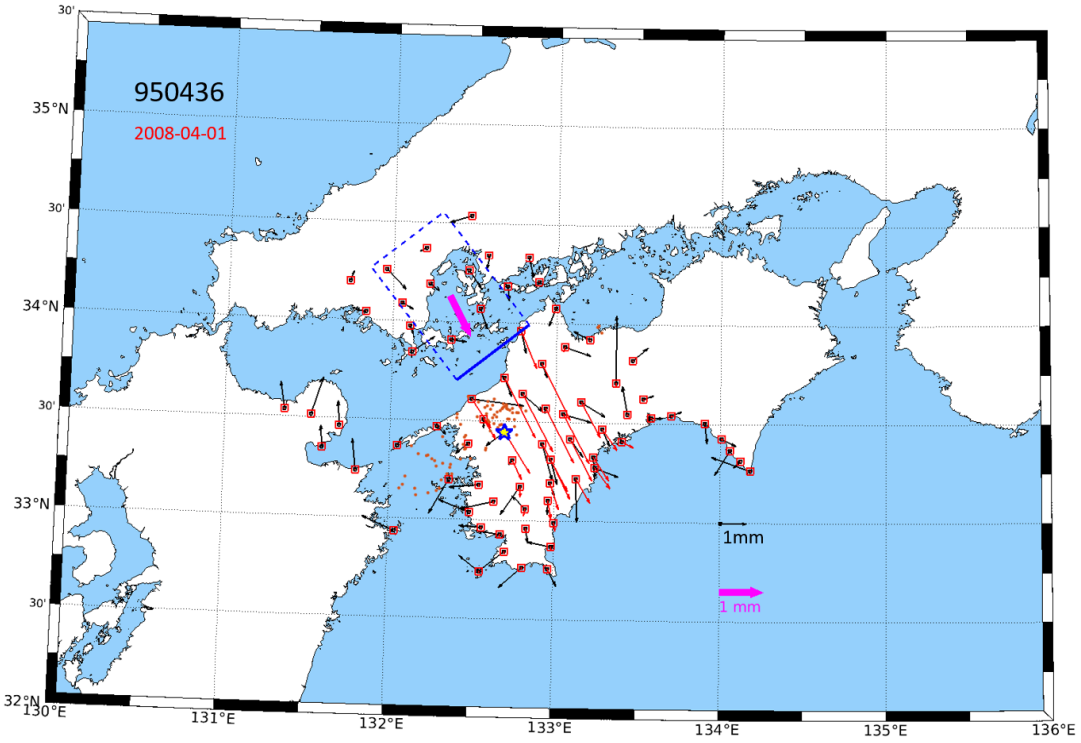

Figure S13. Same as Fig. S4 but for a probable SSE candidate at station 950436.

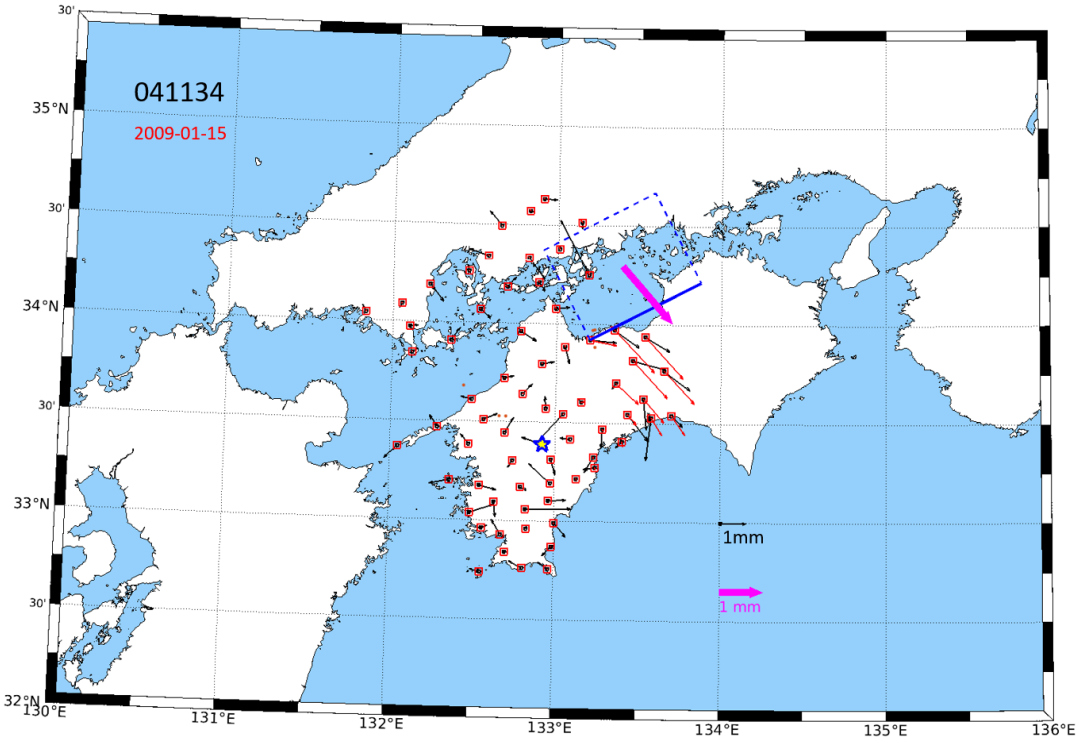

Figure S14. Same as Fig. S4 but for a probable SSE candidate at station 041134.

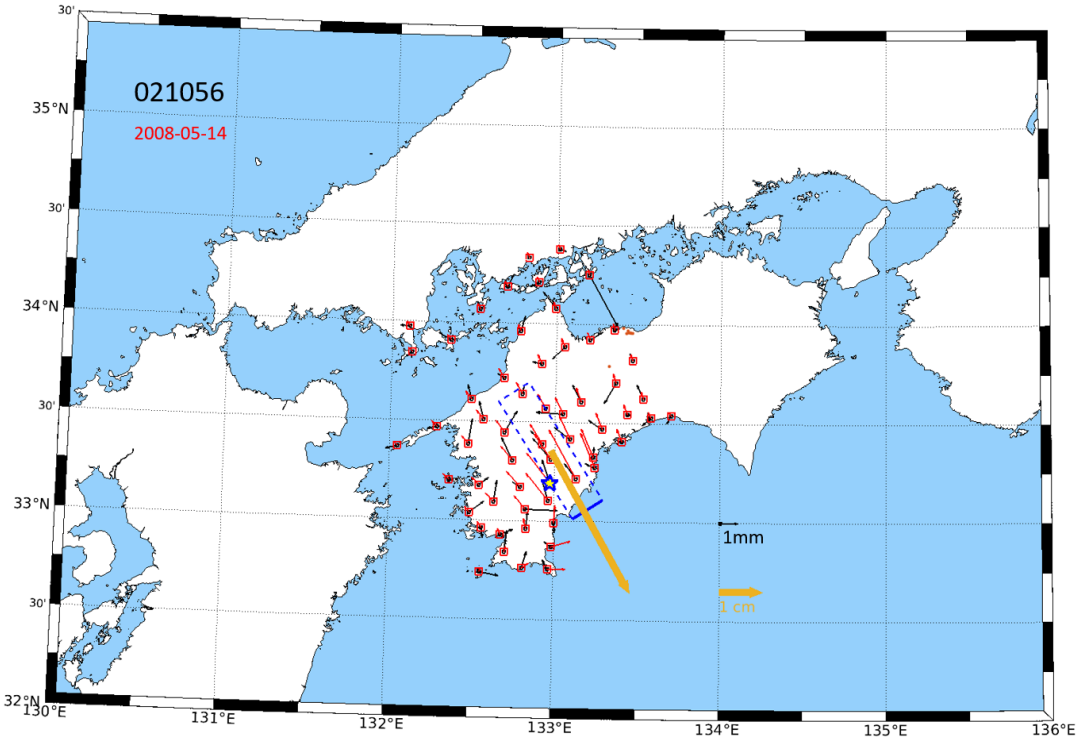

Figure S15. Same as Fig. S4 but for a probable SSE candidate at station 021056.

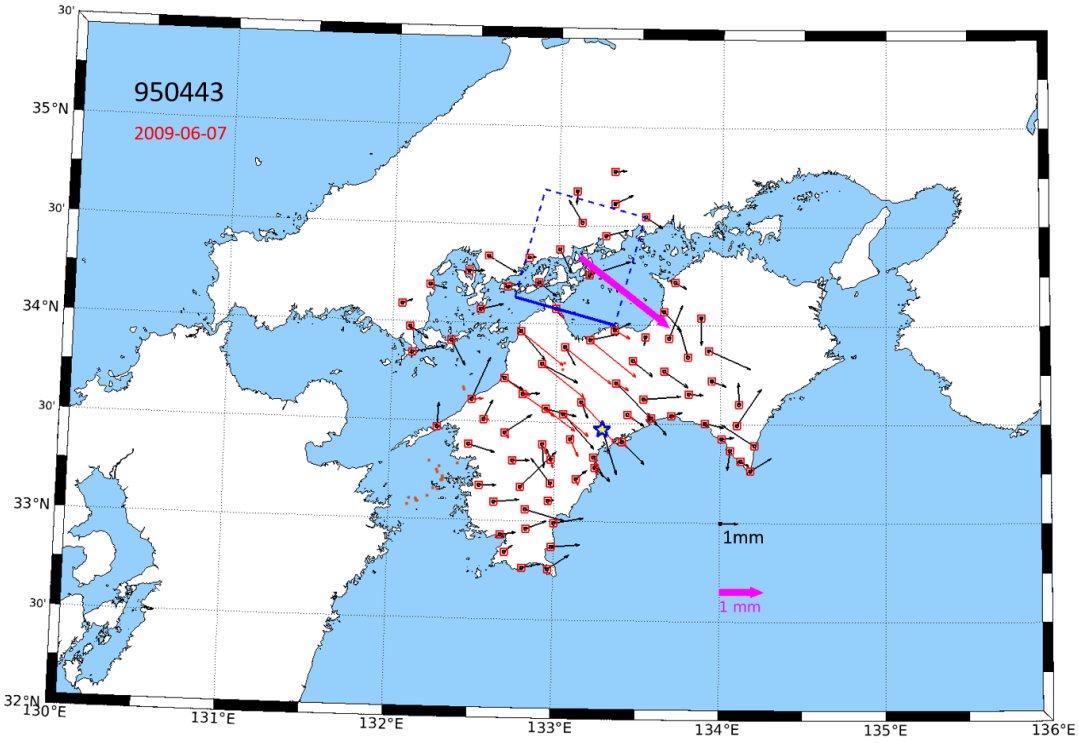

Figure S16. Same as Fig. S4 but for a probable SSE candidate at station 950443.

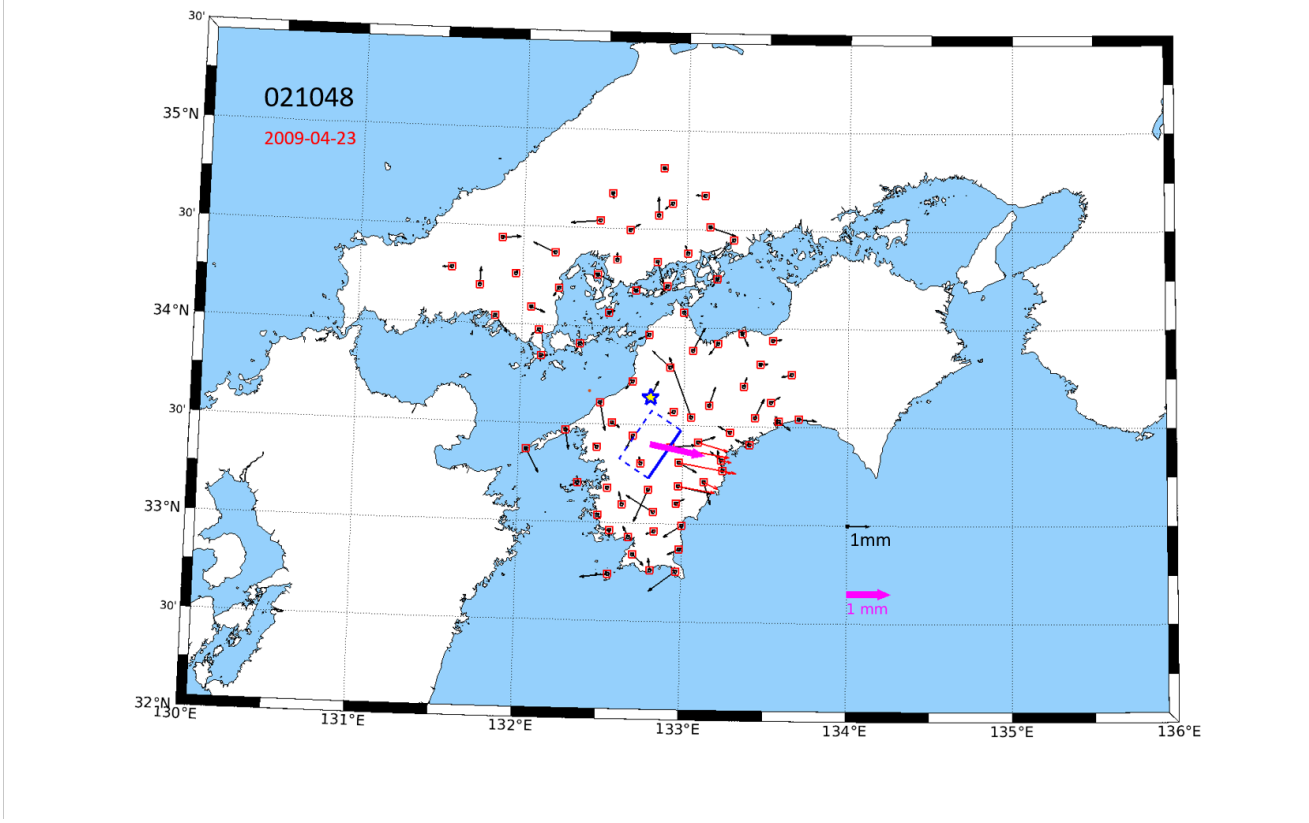

Figure S17. Same as Fig. S4 but for a probable SSE candidate at station 021048.